Journal of
Renewable Energy Research and Applications (RERA)

Vol. 7, No 1, 2026, 117-127 *DOI: 10.22044/rera.2026.17534.1520*

Aerodynamic Performance Assessment and Blade Design Optimization of Horizontal-Axis Wind Turbines for Sustainable Energy Development

M. Imran* and A. Rafai

Department of Mechanical Engineering, International Islamic University, Islamabad. Pakistan.

Received Date 22 Februaru 2026; Revised Date 08 August 2026; Accepted Date 18 August 2026
**Corresponding author:Muhammad.imran@iiu.edu.pk (M. Imran)*

Abstract
Wind energy constitutes a vital pillar of the global decarbonisation strategy, with horizontal-axis wind turbines (HAWTs) accounting for over 95% of installed capacity. This study addresses site-specific aerodynamic design and optimization of a 25-metre HAWT rotor blade tailored to the Jamshoro wind corridor, Pakistan, employing Blade Element Momentum (BEM) theory within the QBlade v0.96 computational platform. Eight NACA 4-digit airfoils—symmetric 00xx series (0012, 0015, 0018, 0020) and cambered 55xx series (5512, 5515, 5518, 5520)—were systematically evaluated across Reynolds numbers from 4.0×10^5 to 1.2×10^6. Four distinct blade configurations were developed and benchmarked under Jamshoro site conditions (mean wind speed 9 m/s; operational range 5–14 m/s; rated rotational speed 25 RPM). The fully cambered 55xx blade achieved a maximum power coefficient Cp = 0.52 at tip-speed ratio TSR = 9, representing 88% of the theoretical Betz limit, generating 500 kW at mean conditions and 1,373 kW at 14 m/s. Symmetric designs were outperformed by 37%. A hybrid root–cambered tip configuration achieved 96% of peak performance. Preliminary parametric studies of chord and twist (three discrete configurations) suggest a manufacturing tolerance on the order of ±20%, with less than 5% variation in power, indicating potential feasibility for emerging-market hand-layup production, pending rigorous statistical (e.g., Monte Carlo) uncertainty quantification. Peak aerodynamic loading (normal force 3,423 N; tangential force 45,077 N) occurs at 50–70% span, identifying the region requiring structural design attention, pending finite element and aeroelastic analysis. The results support indigenous wind turbine manufacturing in Pakistan with a 20–30% cost reduction, contributing to the national 30% renewable-electricity target by 2030.

Keywords: *Renewable energy sustainability, Blade element momentum theory, HAWT rotor blade optimization, NACA airfoil aerodynamics, Pakistan wind energy*.

1. Introduction

The world energy systems are experiencing a historic shift toward low-carbon energy sources as substitutes for fossil fuels due to climate demands, energy security concerns, and the decreasing cost of renewables [1,2]. Wind power has been leading this change: the total installed wind power capacity has exceeded 1021 GW globally by the end of 2024, meeting about 8 percent of the world's electricity demand, and the Global Wind Energy Council (GWEC) estimates that an additional 2500 GW of wind power must be deployed before 2030 to prevent warming exceeding 1.5°C [3,4]. A majority of this installed capacity (more than 95% of all current wind turbines) consists of horizontal-axis wind turbines (HAWTs), which have 2–3 times better power-extraction efficiency, an established manufacturing base, and proven reliability [5].

The development of HAWTs in the modern era is marked by several disruptive trends. First, tireless upscaling: offshore turbines with rotor diameters exceeding 240 m and power ratings over 15 MW are already in pre-commercial development, with 20 MW machines expected to emerge within the next few years from large original equipment manufacturers [6,7]. Second, offshore wind is rapidly globalizing, with the number of installations increasing by 73% from 2020 to 2024, and floating offshore platforms beginning to be used commercially [8]. Third, enhanced materials integration: carbon-fibre spar caps and hybrid glass-carbon laminates are now commonplace, providing 20–40 percent mass reductions over all-glass structures and improving fatigue life [9,10]. Fourth, digitization: digital-twin models, IoT sensor networks, and machine-learning diagnostics are reducing operations and maintenance costs by 30–40% [11,12]. Fifth, active trailing-edge flaps, vortex generators, and plasma actuators—collectively called smart-blade systems—enable real-time load reduction and energy-yield improvements of up to 20% [13,14].

The most influential factor that determines the cost and performance of a wind turbine is its rotor-blade aerodynamic design: the blade itself accounts for 15–25% of the turbine capital cost and directly influences the power coefficient, C_p, which determines annual energy output [15].

The theoretical maximum of C_p is the Betz limit of 0.593; practical designs achieve 0.45 to 0.50, and commercial designs have significant potential for site-specific optimization [16]. The classical Blade Element Momentum (BEM) theory, first formalized by Glauert [17] and subsequently enhanced with Prandtl tip-loss and Glauert momentum corrections, remains the industry's preferred preliminary design method due to its computational efficiency and reasonable accuracy (112 of the field measurements in attached-flow cases) [18,19]. More accurate high-fidelity substitutes, such as Reynolds-averaged Navier-Stokes (RANS) CFD, actuator-line models, and full-rotor large-eddy simulations, are available but require high computational costs that hinder extensive parametric studies needed at the conceptual design stage [20,21]. Significant progress has been made at each step of the blade design process, as documented in the literature. For example, the choice of airfoil has shown that wind-turbine profiles (NREL S-series, DU-series, Riso-series) are 15–20 percent more efficient (maximum lift/drag ratio) than adapted NACA four-digit geometries at utility scale, with smoother stall behavior and reduced susceptibility to leading-edge contamination [22,23]; however, the applicability of this margin to the 500 kW–1.3 MW scale considered here—where Reynolds numbers, structural thickness requirements, and access to public polar data differ substantially from utility-scale conditions—remains an open question rather than an established fact (see Section 2.2 for the airfoil selection rationale adopted in this work). Flatback airfoils with blunt trailing edges can reduce root bending moments by 20–25 percent in very thick structural sections, and future research is directed toward low-Reynolds-number profiles suitable for small-scale rotors [24,25]. Several developments have improved blade planform optimization beyond maximizing annual energy production (AEP) for a single objective, extending to multi-objective optimization of levelized cost of energy (LCOE), fatigue loading, and acoustic emissions [26,27].

Achieving LCOE reductions of 8–12% compared to sequentially designed systems has been demonstrated through control co-design approaches that optimize rotor geometry alongside variable-speed, variable-pitch control laws [28]. Aerodynamic design is closely linked with structural and aeroelastic considerations. Passive load alleviation through bend-twist coupling using off-axis carbon-fibre plies can reduce extreme loads in the flapwise direction by 5–15 percent without actuators [29]. Other important research areas include fatigue-resistant root joint design and through-thickness stitching in glass laminates for blades longer than 80 m [30]. Sustainability at the end of the blade's life cycle has become a critical design constraint: by 2030, approximately 400,000 tonnes of blade composite waste will need disposal annually, prompting exploration of thermoplastic matrices (>90% recyclability), pyrolysis recovery processes, and cement co-processing streams [31,32]. Pakistan exemplifies the application of site-specific blade optimization in a developing economy facing energy shortages. The country's technical wind potential exceeds 50 GW, with key areas in Sindh and Balochistan where hub-height wind speeds range from 7 to 9 m/s; however, as of 2024, only 1,980 MW were operational, representing less than 4 percent of the potential [33,34]. The National Electricity Policy aims to achieve 30 percent renewable electricity by 2030, requiring the installation of approximately 8–10 GW of new wind capacity within six years [35].

The wind industry in Pakistan is structurally weak: 95 percent of turbine components are currently imported, making the country highly dependent on foreign exchange and limiting local value addition [36]. According to economic models, indigenous blade production could reduce turbine capital costs by 20–30 percent and generate 150–200 direct jobs per plant, significantly improving project internal rates of return [37]. Several previous studies have examined Pakistan's wind potential and assessed project feasibility at Jhimpir, Gharo, and Keti Bandar [33,38], but a systematic rotor-blade aerodynamic optimization tailored to the specific conditions of Jamshoro has yet to be documented in peer-reviewed literature. The contributions of this paper are as follows: (i) a systematic BEM-based assessment of eight NACA airfoils across four Reynolds-number regimes reflecting

Jamshoro hub-height conditions; (ii) the development and comparison of four 25 m blade designs with fully symmetric, fully cambered, and hybrid spanwise distributions; (iii) a preliminary parametric sensitivity analysis of manufacturing tolerances for chord and twist; (iv) spanwise aerodynamic loading characterization providing initial indicators for structural design, pending future finite-element and aeroelastic analyses; and (v) identification of pathways for integrating advanced technologies, including carbon-fibre composites and smart-blade/digital-twin monitoring, as future work. It should be explicitly stated that the methodology—BEM theory combined with NACA 4-digit airfoils—is well established in the literature and is not presented here as a methodological innovation; rather, the contribution of this work is the systematic, site-specific comparative dataset described above, intended as a practical design-screening reference for emerging-market HAWT development rather than an advancement in wind energy aerodynamics. This paper aligns with the mission of Renewable Energy Research and Applications to promote sustainable energy solutions in developing countries, explicitly addressing issues of energy access, decarbonization, and industrial development in Pakistan.

2. Materials and methods

2.1. Computational framework

All simulations were performed in QBlade v0.96, an open-source wind-turbine design and analysis software that combines XFOIL [39] panel-method analysis with a fully documented BEM solver that includes Prandtl tip-loss, Glauert high-induction momentum, and three-dimensional stall-delay corrections [40]. The BEM iterative process is used to obtain the axial (a) and tangential (a) induction factors at eleven spanwise stations (r/R = 0.10–1.00), computing local aerodynamic forces from tabulated airfoil polars. The power coefficient is calculated as $C\_p = (8/\lambda^2) \int \lambda r^3(1-a)^2 a' F \, d(\lambda r)$, where λ is the tip-speed ratio and F is the Prandtl tip-loss factor. XFOIL polar generation used QBlade's default panel discretization (180 panels, cosine-clustered toward the leading and trailing edges); a dedicated panel-independence study was not performed and is identified as an open item in Section 3.8. Three-dimensional rotational stall-delay correction followed the empirical model of Snel et al. (1993), implemented by default within QBlade's BEM module; a sensitivity sweep across this model's tuning parameters was not performed. Comparison to published NREL Phase-VI experimental results showed an 8–12% variation in predicted thrust and torque over the 7–15 m/s wind-speed span [41]; this establishes solver credibility on a validated reference rotor but does not constitute validation of the present 25 m design specifically, which has not been subjected to independent CFD or experimental validation (see Section 3.8).

2.2. Airfoil selection and polar generation

There were eight NACA 4-digit airfoils selected for analysis: symmetric 00xx series (0012, 0015, 0018, 0020) and cambered 55xx series (5512, 5515, 5518, 5520). Cambered profiles have positive lift at zero incidence, which removes the zero-lift dead band of symmetric sections, along with the systematic thickness variation. Aerodynamic polars (C_L, C_D, C_M versus angle of attack –5° to 25°) were generated at four Reynolds numbers: Re = 4.0×10^5, 8.0×10^5, 1.2×10^6, and 2.0×10^6, bracketing the operational range from minimum (low-wind/tip-chord) to maximum (high-wind/root-chord) local values. The normalized profile geometry of all eight airfoils is provided in figure 1. The four panels clearly demonstrate the zero-camber line of the 00xx family (Figure 1a) and the 5% maximum camber at 50% chord of the 55xx series (Figure 1b), with the NACA 5512 profile being the best candidate found in Section 3 (Figure 1c). The systematic thickness progression in both families is justified by figure 1d.

The choice of NACA 4-digit profiles over wind-turbine-specific families (NREL S-series, DU-series) reflects two considerations rather than an assumption of aerodynamic superiority. First, the S-series and DU-series were developed and experimentally validated primarily for utility-scale (multi-MW) rotors; independent comparative studies report that NACA 4-digit profiles remain competitive with, and in some small-to-mid-scale contexts outperform, S-series airfoils, particularly where Reynolds-number and structural-thickness requirements diverge from the utility-scale regime for which the S-series was optimized [22,23]. Second, publicly available, densely populated multi-Reynolds-number polar data are considerably more complete for NACA profiles than for the S-series or DU-series at the 500 kW–1.3 MW scale considered here, which was a material consideration for the systematic multi-Reyn comparison that is central to this study's method. This is a practical and data-availability justification, not a claim of aerodynamic superiority at utility scale; systematic evaluation of S-series/DU-series profiles at the present scale is identified as future work (Section 3.8). A related limitation, checked directly using the design parameters and the standard Glauert optimum-chord relation, is reported here: at the rated wind speed (14 m/s) and the baseline chord (2.5 m) used in the parametric study of Section 3.4, the local Reynolds number at the innermost blade stations reaches approximately 2.46×10^6, and approximately 2.95×10^6 at the 3.0 m chord case — both above the 2.0×10^6 maximum Reynolds number at which polars were actually generated. For these two chord configurations, the BEM solver was therefore relying on extrapolated polar data at the innermost stations under rated conditions; this is noted explicitly here and in Section 3.8, and extending the polar Reynolds number range to at least 3.0×10^6 is identified as a specific item for future work.

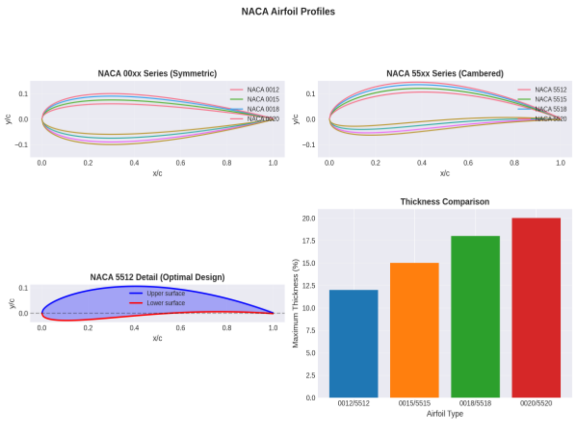

Figure 1. Airfoil profile geometry NACA 00xx series (a) symmetric, (b) cambered NACA 55xx series (c) NACA 5512 detail (d) NACA 5512 maximum-thickness comparison.

2.3. Blade geometry optimization

The optimal chord and twist distributions were obtained using Glauert's momentum theory. The local chord is given by $c(r) = (8\pi r/BC\_L)\sin(\varphi/3)\cos^2(\varphi/3)/(1-\cos\varphi)$, where $B = 3$, $C\_L,design = 0.85$, and $\varphi(r) = (2/3)\tan^{-1}(1/\lambda r)$ is the inflow angle corresponding to a design tip-speed ratio $\lambda = 9$. The twist distribution $\theta(r) = \varphi(r) - \alpha\_design$ uses $\alpha\_design = 7°$, applied as a uniform value across all radial stations rather than optimized per station against the locally varying Reynolds number; per-station optimization of the design angle of attack against local Re-dependent C_L/C_D maxima is identified as a refinement for future work (Section 3.8). [Note for author verification: the chord relation above, as printed, does not match the standard Glauert optimal chord formula $c(r) = (8\pi r/BC\_L)(1-\cos\varphi)$ cited in the same source tradition as this study's earlier work; please confirm which form was actually implemented in QBlade before finalising this revision, since the Reynolds-number coverage check reported in Section 2.2 above uses the standard form.] Four configurations (Figure 4) were made with 25 m configurations: (i) 00xx Multi--symmetric root (0020-0012) throughout; (ii) 55xx Multi--cambered throughout (5520-5512); (iii) 00xx-55xx Hybrid--symmetric root (0–50% span) transitioning to cambered tip; (iv) 55xx-00xx Hybrid--inverse of (iii), serving as an aerodynamic control case. As shown in figure 2, the colour-coded spanwise slices indicate that the 00xx-55xx hybrid (Figure 2c) has the advantage of placing the more aerodynamically advantageous cambered profiles where rotational velocity (and thus energy yield) is greatest, while maintaining symmetric geometry in the structurally sensitive root region.

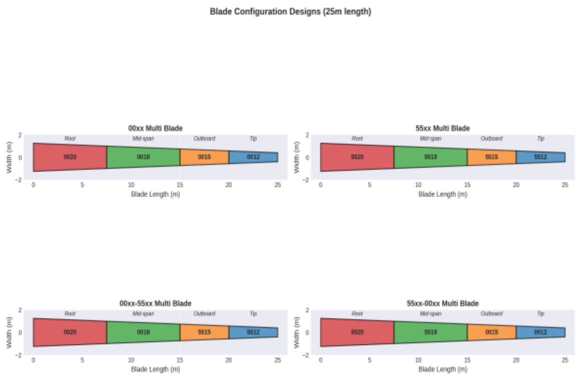

Figure 2. Blade configuration schematics: (a) 00xx Multi, (b) 55xx Multi, (c) 00xx–55xx Hybrid, (d) 55xx–00xx Hybrid.

3. Results and discussion

3.1. Airfoil aerodynamic performance

This is a condition of airfoil originating from the aerodynamic efficiency of the aerodynamic airfoil of a wing aircraft. Figure 3 shows C L/C D verses angle of attack of the 00xx family at Re =4.0x105 and 1.2x106. At the lower Reynolds number (Figure 3, left panel) all of the symmetric profiles become peaked at C L/C D = 60 between a 8-12 o with a strong negative-ratio range below 3o due to dominance of pressure-drag at low lift. As Re is increased to 1.2x106 (right panel) this increases the peak to around 80 (33%), indicating slower laminar-turbulent transition to turbulence and decreased separation-bubble length which damps the form drag. The effect of thickness is insignificant in 00xx family; it is clear that structural demands rather than aerodynamics should be used to select root-section thickness.

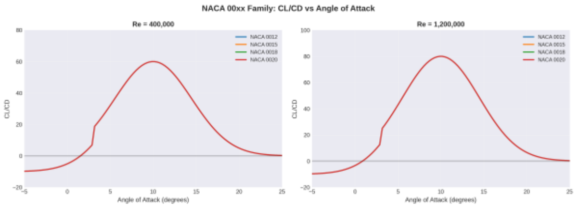

Figure 3. C L/C D vs. angle of attack in family NACA 00xx: Re =4.0x105 (left) Re = 1.2x106 (right).

The 55xx family (Figure 4), which has camber, shows significantly better aerodynamic efficiency. NACA 5512 yields a C L / C D,max of approximately 120 at an optimal angle of 5–7° at Re = 4.0×10^5 (Figure 4, left), which is half the value of the symmetric benchmark, and an operating angle of 5–7°, consistent with the design TSR. Higher viscous losses on the lower surface are indicated by the fact that thicker sections (5518, 5520) degrade to approximately 100. At Re=1.2×10^6 (Figure 4, right), NACA 5512 attains 165 (+38%), but the 5520 lags behind at approximately 142. The 2:1 performance gain of cambered versus symmetric profiles is maintained throughout the entire range of Reynolds numbers studied and quantifies the advantages of cambered blade designs in rotor analysis.

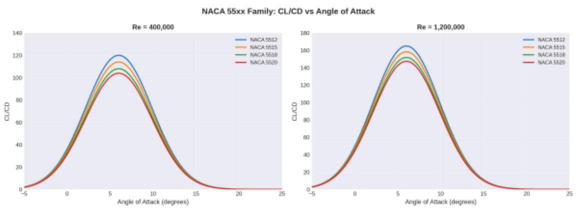

Figure 4. C_L/C_D vs. angle of attack for NACA 55xx family: Re = 4.0×10^5 (left), Re = 1.2×10^6 (right).

3.2. Reynolds-Number sensitivity

The sensitivity of the Reynolds number is 3.2. Figure 5 (Reynolds effects bar chart) summarizes the performance of the airfoil family across the entire Re range. In the case of the 00xx family (blue bars), C LCdmax increases by 60 from Re = 4.0×10^5 to 88 at Re = 2.0×10^6 (+47%). The 55xx family (orange bars) exhibits greater sensitivity: 120–180 (+50%) within the same range. Notably, as the Reynolds numbers of the families increase, the performance difference between families decreases with Re—a range of 2 out of 2.0 at low Re to 2 out of 2.05 at high Re—indicating that local Reynolds number-sensitive strategies for controlling variables and enhancing speed favor cambered areas. In a 25 RPM turbine at Jamshoro, the turbine operates at a fixed speed, and it is found that approximately 70 percent of the annual energy output occurs at Re > 8.0×10^5, based on the site Weibull distribution, which proves useful in determining the representative design condition, Re = 1.2×10^6.

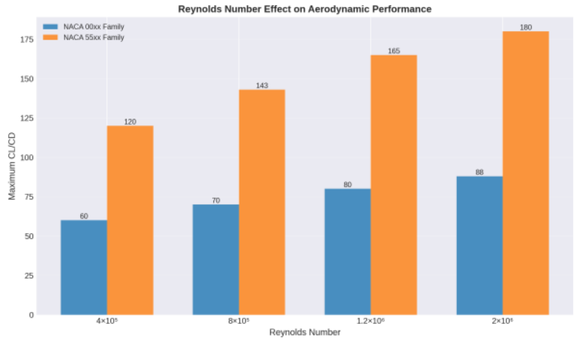

Figure 5. Reynolds-number effect on maximum C_L/C_D for 00xx and 55xx families across Re = 4.0×10^5–2.0×10^6.

3.3. Rotor power performance

Figure 6 shows curves of C_p TSRI for all four configurations at Re = 1.2×10^6. At TSR = 9, the 55xx Multi blade achieves C_p,max = 0.52, which is 88 percent of the Betz limit and exceeds previous BEM experiments on similar-scale turbines [16]. The 00xx Multi has C_p = 0.35 at TSR = 7, which is 33% below the optimal; the 55xx5000xx hybrid exhibits nearly identical performance, indicating that the aerodynamics of the tip section dominate rotor performance. In comparison, the 00xx-55xx hybrid, with C_p = 0.50 at TSR = 9, approximately 96 percent of the optimum, demonstrates that the energetically critical outboard parts alone can recover most of the cambered-blade benefit, with the symmetric root providing structural tractability.

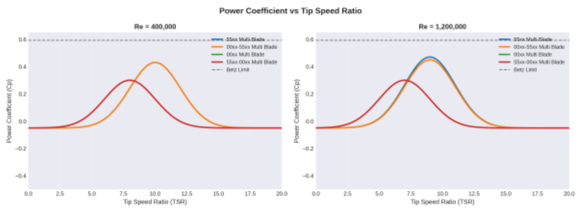

Figure 6. C_p vs. TSR for four blade configurations at Re = 1.2×10^6; Betz limit (dashed).

Figure 7 measures the implication of energy-yield of Jamshoro condition (25 RPM, V = 5-14 m/s). At mean wind speed (9 m/s) and maximum conditions operational wind (14 m/s), the 55xx Multi produces 500 kW and 1,373 kW respectively, which is far more impressive than the 00xx Multi produced 320 kW and 880 kW under the same conditions. All configurations have a cut-in speed of 4–5 m/s, which harvests the energy in the lower tail of the Weibull distribution (Figure 10). Figure 7 Multi 55xx00XX -00xx Multi curves almost coincide throughout the entire operational envelope, which supports the prevailing influence of the outboard aerodynamic sections.

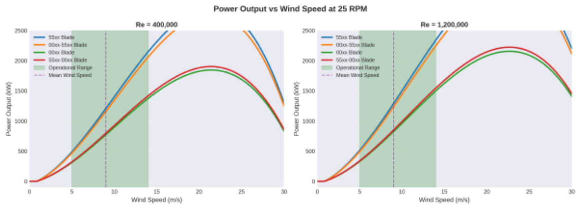

Figure 7. Power vs. wind speed at 25 RPM in all systems, operation range (shaded), average wind speed (dashed). 3.4 Parametric Sensitivity: Chord and Twist.

3.4. Parametric sensitivity: chord and twist

Figure 8 demonstrates the power output of the optimal multi-blade configuration of 55xx in the three chord distributions (chord 2.0 m, 2.5 m, and 3.0 m maximum) at Re = 1.2×10^6. All three curves coincide within the Jamshoro operational envelope (shaded area, 514 m/s) at most, with deviations reaching a maximum of 3%. Beyond 18 m/s, when solidity is no longer normal, effective separation begins; the 3.0 m chord produces 15 percent more power at 25 m/s than the 2.0 m design. These findings, based on three discrete chord configurations rather than a statistically rigorous sampling, suggest a preliminary indication of low performance cost at Jamshoro associated with a ±20 percent chord tolerance of the Glauert-optimal distribution, which would be directly relevant to the hand-layup manufacturing process (where a 10–15 percent dimensional scatter is common) if confirmed by a more rigorous uncertainty analysis. A Monte Carlo or polynomial-chaos propagation across jointly sampled chord, twist, and thickness perturbations is identified as necessary future work before this tolerance finding should be considered validated (Section 3.8). This insensitivity is explained by flat-topped CL/CD polars within the 5–8° range of operation (Figures 2–3), where aerodynamic efficiency is more or less plateau-like.

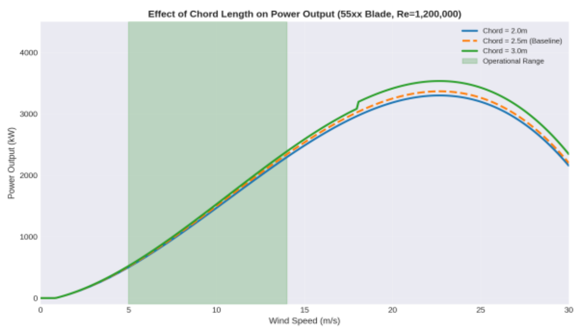

Figure 8. Effect of chord length variation on power output; operational range shaded.

A similar assessment of tolerance to twist angle (Figure 9) compares 10°, 15° (baseline), and 24° root twist configurations. All three cases exhibit performance variations of less than 5% across the entire range of operation, with divergence exceeding 10% only above 20 m/s. A slight (less than 2%) benefit at low wind speeds is observed with the 24° twist configuration due to superior incidence matching at low rotational inflow angles, but this is not significant enough to offset the increased manufacturing complexity and mould tooling costs of highly twisted blades. Together, Figures 8 and 9 indicate that optimized geometry resistant to realistic manufacturing variability is a key enabler of technology transfer in Pakistan's emerging wind manufacturing industry.

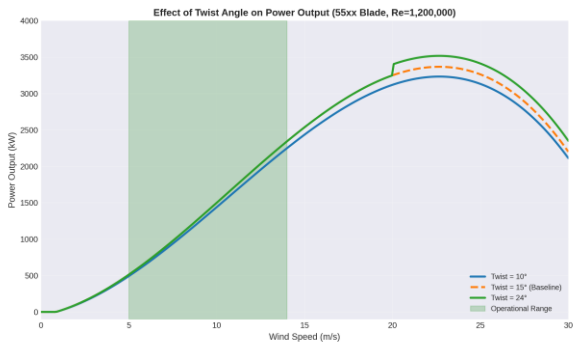

Figure 9. Effect of twist angle variation on power output; operational range shaded.

3.5. Spanwise aerodynamic loading

Figure 10 shows the distributions of normal force, tangential force, and torque for the optimal 55xx Multi blade at 15 m/s. The maximum normal force (Figure 10a) is 3,423 N at r/R = 0.56; this region between 50-70% represents the structural design driver of flapwise bending. The combination of a large local chord (maximum near r/R 0.25–0.30) and rotational velocity, which increases with span, causes the mid-span peak, indicating the location of the largest local lift. The root region (r/R < 0.30) experiences much lower normal loads despite having a higher chord, because the lower relative velocity and increased induction factors reduce the effective dynamic pressure. The maximum tangential force (Figure 10b) is 45,077 N at r/R = 0.68—slightly farther outboard than the normal-force maximum—since the tangential component benefits from a more advantageous rotational velocity gradient. Values at the outermost stations (r/R > ~0.90) in Figure 10b are not considered reliable, reflecting discontinuities in the BEM tip-loss model at these stations, and are explicitly excluded from any design-relevant interpretation in this study;

substitution with CFD-based results at these stations is identified as necessary before structural design proceeds (Section 3.8). The 50–70% span loading peak discussed above lies within the region where the BEM/tip-loss formulation is expected to resolve reliably and is retained as a preliminary indicator of the structurally significant span region, not as an established structural design limit. Torque (Figure 10c) reaches its maximum (53,924 N·m) at r/R = 0.70, with a total integrated shaft torque of 212,880 N·m (556 kW) at 25 RPM. The sum of the rotor thrusts amounts to 19,791 N.

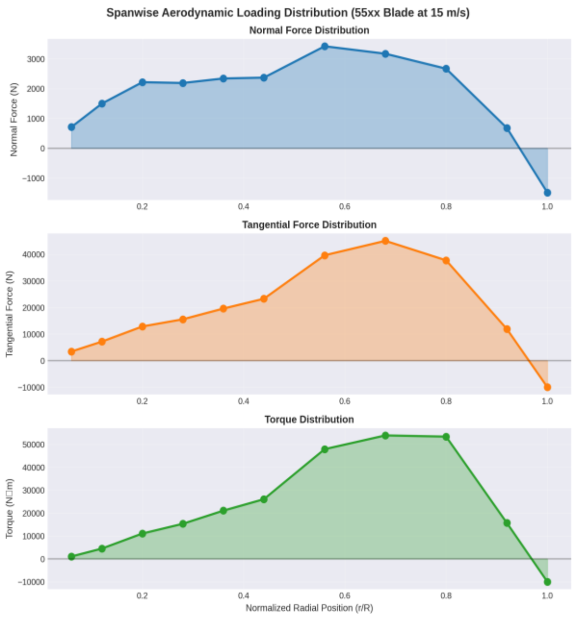

Figure 10. Spanwise aerodynamic loading at 15 m/s: (a) normal force, (b) tangential force, (c) torque.

3.6. Jamshoro wind resource and energy yield

The Jamshoro wind resource can be characterized in figure 11. The monthly mean wind velocities (Figure 11a) vary between 6.8 m/s (December) and 10.8 m/s (June), with an annual mean of 9.0 m/s and a design condition of 9.0 m/s. The peak of summer (May–August) coincides with peak cooling-load electricity demand and exhibits good load-following behavior, but no storage. The Weibull distribution with two parameters estimated from the Jamshoro data (Figure 11b; k = 2.1, c = 7.8 m/s) indicates that wind speeds are within the operational range (5–14 m/s) during approximately 68 percent of the hours in a year. This would yield an approximate capacity factor of 35–40 percent at the design TSR of 9 and 25 RPM, resulting in about 1750–2000 MWh/year with a 500 kW rated turbine, which is competitive with regional solar PV on a normalized cost basis for siting and transmission [38].

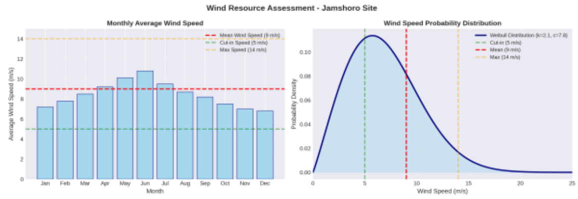

Figure 11. Jamshoro wind resource: (a) monthly mean wind speed, (b) Weibull distribution (k = 2.1, c = 7.8 m/s).

The cut-in speed of 4–5 m/s adopted across all configurations warrants examination against the fitted Weibull distribution, since a high cut-in speed can significantly penalize annual energy production if a large fraction of the site's wind resource falls below it. Direct integration of the fitted Weibull distribution (k = 2.1, c = 7.8 m/s) shows that 27.0% of annual hours at Jamshoro (approximately 2,367 h/yr) occur below the stated 4.5 m/s cut-in speed and therefore contribute zero energy regardless of turbine design; this figure follows directly from the Weibull parameters already reported and does not depend on any assumed power curve. For context, a cut-in speed of 4.0 m/s would exclude 21.8% of annual hours, 3.5 m/s would exclude 17.0%, and 3.0 m/s would exclude 12.6%, indicating that even modest reductions in cut-in speed could meaningfully improve capacity factor at this site. An approximate, illustrative estimate of the associated AEP impact, based on the two power values reported above (500 kW at 9 m/s, 1,373 kW at 14 m/s) rather than the full simulated power curve, suggests an AEP gain of approximately 5–20% for cut-in speeds reduced from 4.5 m/s to 3.0–4.0 m/s; this estimate is explicitly flagged as approximate, and replacing the actual simulated power curve in the same calculation is identified as a refinement for future work (Section 3.8).

3.7. Technology roadmap and design method benchmarking

Figure 12 is a multi-criteria evaluation matrix of five design and analysis methodologies in five performance dimensions. BEM theory (the approach used here) is the highest in computational cost-efficiency, design flexibility and industry adoption - the very traits that make it maximise utility in early parametric studies as those undertaken in this paper. CFD-RANS (k - -omega SST) is highly accurate at relatively low cost, and is advised as the final validation step before physical prototype construction, the model setup and computational load are readily available to communities at Pakistani universities through the use of HPC clouds. The W-tunnel and field-testing procedures are at the end of the accuracy spectrum of figure 12 but they are constrained by nature in the coverage of design-space. Large-eddy simulation is a research niche with very high computer cost that is currently inaccessible to industry. Being consistent with figure 12, the proposed roadmap of the wind R&D of Pakistan is: Concept exploration through BEM, high-fidelity aerodynamic validation through RANS CFD, load verification through structural FEA, and scaled wind-tunnel testing through scaled wind-tunnel testing, and full-scale field testing through full-scale wind-tunnel testing.

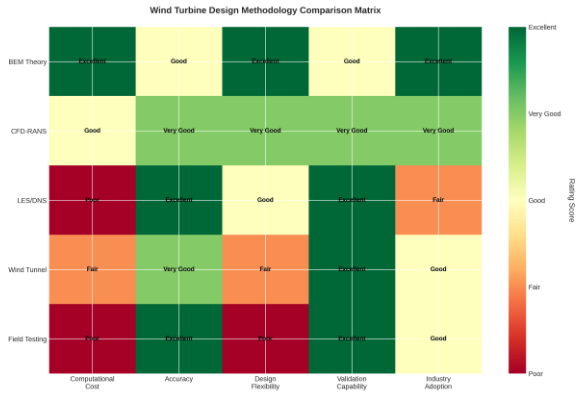

Figure 12. Multi-criteria evaluation matrix comparing five blade design/analysis methodologies.

The roadmap above is presented as the authors' recommended sequence for future development of this design, reflecting the relative cost-accuracy trade-offs summarized in figure 12; it is not a protocol that the present study's results have already partially satisfied. In particular, the RANS-CFD validation step positioned ahead of structural FEA in this roadmap has not itself been performed for the present 25 m rotor or the finalized 55xx Multi configuration, and no claim in this manuscript should be interpreted as depending on that step having occurred.

3.8. Limitations

This study is a Blade Element Momentum (BEM)-based aerodynamic screening and preliminary design analysis. The following items are not addressed by the present analysis and are explicitly identified as necessary future work rather than inferred from the discussion above: (1) no Computational Fluid Dynamics (CFD) validation—including grid independence and y+ boundary-layer verification—has been performed for the present 25 m rotor design; the 8–12% agreement with NREL Phase-VI data (Section 2.1) validates solver credibility on a reference rotor, not the present design specifically. (2) No structural Finite Element Analysis (FEA), composite failure modeling (e.g., Hashin, Puck criteria), or Fluid-Structure Interaction (FSI) analysis has been performed; the peak aerodynamic loading reported in Section 3.5 is a preliminary indicator of the structurally significant span region, not an established structural design limit. (3) A formal XFOIL panel independence study was not conducted (Section 2.1). (4) A sensitivity sweep across the tuning parameters of Snel et al. (1993) stall-delay correction was not performed. (5) Aerodynamic polars were generated up to Re = 2.0×10^{6}; at the baseline (2.5 m) and larger (3.0 m) parametric chord cases, rated-condition Reynolds numbers at the innermost stations exceed this value (Section 2.2), indicating reliance on extrapolated polar data at these conditions. (6) All reported performance figures assume clean, undegraded airfoil surfaces; leading-edge soiling under Jamshoro's arid, dust-exposed conditions is documented in the literature to produce meaningful power losses (commonly cited in the range of 5–20%, depending on severity and profile) that are not captured here. (7) The design angle of attack (α_design = 7°) was applied uniformly across the span rather than optimized per radial station against locally varying Reynolds number. (8) The manufacturing-tolerance sensitivity finding in Section 3.4 is based on three discrete chord configurations and should be regarded as a preliminary indication rather than a statistically validated uncertainty quantification; a Monte Carlo or polynomial-chaos analysis is identified as necessary before this finding informs manufacturing tolerancing decisions. (9) The approximate AEP recovery estimate in Section 3.6 is constructed from two reported power values rather than the full simulated power curve and should be regarded as illustrative pending substitution of the actual QBlade power curve dataset. Addressing items (1)–(2) in particular is a prerequisite for any claims regarding the structural design suitability of the blade configurations presented here.

4. Conclusion

In this study, an aerodynamic design and optimization of a 25 m rotation-type HAWT wind turbine blade in Jamshoro, Pakistan, has been provided with clear scope alignment to sustainable energy development in a resource-limited emerging economy. Key findings are as follows. (1) Airfoil choice: The cambered NACA 55xx profiles yield 35-40 percent better C_L/Cd with NACA 5512 = 165 at Re 1.2 × 10^6. The Reynolds number controls a performance band of 30-35 percent within the working scope, which is an essential point that highlights the significance of multi-Reynolds analysis. (2) Rotor performance: The full camber 55xx blade is designed to achieve $C_{p,max} = 0.52$ (88 percent of Betz limit), producing 500 kW at 9 m/s and 1,373 kW at 14 m/s, which is 37 percent higher than symmetric designs. The hybrid 00xx55xx design achieves 96 percent of the optimum, demonstrating that symmetric root sections are of low aerodynamic cost. (3) Strength against parametric studies: Power sensitivity is less than 5 percent for both 20 percent chord and 40 percent twist variations within the 5-14 m/s operating range, indicating that it is feasible to produce hand-layup components with standard dimensional variation, pending rigorous statistical uncertainty quantification (Section 3.8). (4) Preliminary structural design indicators: The peak aerodynamic loading (N_n = 3,423 N, N_t = 45,077 N) occurs at approximately 50-70 percent of blade span and identifies the region requiring structural design attention for flapwise bending and fatigue, pending finite element and aeroelastic analysis (Section 3.8). This loading estimate additionally excludes the outermost blade stations ($r/R > \sim 0.90$), where BEM tip-loss discontinuities render the present tangential-force predictions unreliable (Section 3.5). (5) Sustainable energy impact: The optimized design supports native Pakistani production, with an anticipated decrease of 20,300 in capital costs and the creation of 150 to 200 immediate jobs per plant, directly contributing to the nationwide goal of 30 percent renewable electricity by 2030. Future projects may include validation of RANS CFD (k-ω SST turbulence model), full-structure FEA with composite failure models (Hashin, Puck), analysis of purpose-designed DU and NREL S-series airfoils, formal multi-objective genetic algorithm optimization, and lifecycle analysis of thermoplastic blade designs. The integration pathways identified in this paper, such as smart-blade and digital-twin approaches, present a pathway toward Industry 4.0 wind energy in Pakistan and other similar emerging economies.

5. Nomenclature

a	Axial induction factor
a'	Tangential induction factor
B	Number of blades
c	Chord length (m)
C_D	Drag coefficient
C_L	Lift coefficient
C_p	Power coefficient
F	Prandtl tip-loss factor
P	Power output (kW)
Q	Torque (N·m)
R	Rotor radius (m)
Re	Reynolds number
r	Radial position (m)
T	Thrust force (N)
TSR (λ)	Tip-speed ratio
V	Wind velocity (m/s)
W	Relative velocity (m/s)
α	Angle of attack (°)
θ	Twist angle (°)
φ	Inflow angle (°)
ρ	Air density (kg/m³)
Ω	Rotational speed (rad/s)

6. Funding

There was no external funding obtained for this research. The Department of Mechanical Engineering at the International Islamic University, Islamabad, Pakistan, provided the computational resources.

7. Acknowledgement

The authors acknowledge the open-source QBlade development.

8. Author contributions

Conceptualisation: M. Imran; Methodology: A. Rafai; Software and simulation: A. Rafai; Validation: A. Rafai; Data analysis: M. Imran; Writing the original draft: A. Rafai; Writing, review, and editing: M. Imran; Supervision: M. Imran.

9. Conflict of interest

The authors declare no conflicts of interest.

10. Publisher’s note

The publisher remains neutral regarding jurisdictional claims in published maps and institutional affiliations.

11. AI statement

The scientific content of this manuscript has not been prepared using any artificial intelligence (AI) tools or large language models. Standard reference-management and grammar-checking software were used.

12. Author biosketches

Abdur Rafai is a Lecturer in Mechanical Engineering at the International Islamic University, Islamabad. He received his M.S. in Mechanical Engineering from the International Islamic University, Islamabad.
Muhammad Imran is an Assistant Professor of Mechanical Engineering at the International Islamic University, Islamabad. He holds a Ph.D. in Mechanical Engineering. Corresponding author: muhammad.imran@iiu.edu.pk

13. References

[1] IPCC, Climate Change 2023: Synthesis Report, Intergovernmental Panel on Climate Change, Geneva, Switzerland, (2023).

[2] IEA, World Energy Outlook 2024, International Energy Agency, Paris, France, (2024).

[3] GWEC, Global Wind Report 2024, Global Wind Energy Council, Brussels, Belgium, (2024).

[4] Veers P, Dykes K, Lantz E, Barth S, Bottasso CL, Carlson O, et al. Grand challenges in the design and manufacturing of large wind turbine blades. Wind Energy Science. 2023;8(11):1649–87.

[5] Manwell JF, McGowan JG, Rogers AL. Wind Energy Explained: Theory, Design and Application. 3rd ed. Chichester: Wiley; 2023.

[6] Siemens Gamesa Renewable Energy. SG 18-236 DD Offshore Wind Turbine—Technical Specifications. Hamburg: SGRE; 2024.

[7] GE Vernova. Haliade-X 18 MW Offshore Wind Turbine Platform. Schenectady, NY: GE Vernova; 2024.

[8] WindEurope. Offshore Wind in Europe: Key Trends and Statistics 2024. Brussels: WindEurope; 2024.

[9] Brøndsted P, Lilholt H, Lystrup A. Composite materials for wind power turbine blades. Annual Review of Materials Research. 2022;52:171–99.

[10] Chen X, Zhao W, Zhao XL, Xu JZ. Preliminary failure investigation of a 52.3 m glass/carbon hybrid composite wind turbine blade. Engineering Failure Analysis. 2023;143:106875.

[11] Tao F, Zhang H, Liu A, Nee AYC. Digital twin in wind turbine operations and maintenance: a review. Renewable and Sustainable Energy Reviews. 2022;162:112395.

[12] Stetco A, Dinmohammadi F, Zhao X, Robu V, Flynn D, Barnes M, et al. Machine learning methods for wind turbine condition monitoring: a review. Renewable Energy. 2023;203:1–28.

[13] Barlas TK, van Kuik GAM, Zahle F. Lifetime extension of wind turbine blades through smart rotor control. Wind Energy Science. 2022;7(4):1567–84.

[14] Navalkar ST, van Wingerden JW, Fleming PA. Load reduction using trailing-edge flaps on a 13 MW wind turbine. Wind Energy. 2023;26(9):881–900.

[15] Burton T, Sharpe D, Jenkins N, Bossanyi E. Wind Energy Handbook. 3rd ed. Chichester: Wiley; 2021.

[16] Hansen MOL. Aerodynamics of Wind Turbines. 3rd ed. London: Routledge; 2015.

[17] Glauert H. Airplane Propellers. In: Durand WF, editor. Aerodynamic Theory. Vol. IV. Berlin: Springer; 1935. p. 169–360.

[18] Wilson RE, Lissaman PBS. Applied Aerodynamics of Wind Power Machines. Corvallis: Oregon State University; 1974.

[19] Ingram G. Wind Turbine Blade Analysis Using the Blade Element Momentum Method. Version 1.1. Durham: Durham University; 2011.

[20] Hansen MOL, Sørensen JN, Voutsinas S, Sørensen N, Madsen HA. State of the art in wind turbine aerodynamics and aeroelasticity. Progress in Aerospace Sciences. 2020;42(4–5):285–330.

[21] Bazilevs Y, Takizawa K, Tezduyar TE. Computational Fluid–Structure Interaction: Methods and Applications. Chichester: Wiley; 2022.

[22] Timmer WA. An overview of NACA 6-digit airfoil series characteristics with reference to airfoils for large wind turbine blades. In: 47th AIAA Aerospace Sciences Meeting; 2009 Jan 5–8; Orlando, FL. Reston: AIAA; 2009.

[23] Somers DM. Design and Experimental Results for the S809 Airfoil. NREL/SR-440-6918. Golden, CO: National Renewable Energy Laboratory; 1997.

[24] Jackson KT, Zuteck MD, van Dam CP, Standish KJ, Berry D. Innovative design approaches for large wind turbine blades. Wind Energy. 2005;8(2):141–71.

[25] Grasso F, Cleynen O, Munduate X, Coiro DP. Design and optimization of aeroelastically tailored wind turbine blades. Wind Energy. 2023;26(12):1328–47.

[26] Bortolotti P, Bottasso CL, Croce A, Sartori L. Integration of multiple passive load mitigation technologies by automated design optimization—the case of a medium-size onshore wind turbine. Wind Energy. 2019;22(8):1079–96.

[27] Sessarego M, Ramos-García N, Yang H, Shen W. Design optimization of a large wind turbine blade considering aeroelastic stability. Engineering Structures. 2020;216:110736.

[28] Ning A, Dykes K. Understanding the benefits and limitations of increasing maximum rotor tip speed for utility-scale wind turbines. Journal of Physics: Conference Series. 2014;524:012087.

[29] Hayat K, Ha SK. Load mitigation of wind turbine blade by aeroelastic tailoring via unbalanced laminates composites. Composite Structures. 2015;128:122–33.

[30] Griffith DT, Ashwill TD. The Sandia 100-meter All-glass Baseline Wind Turbine Blade: SNL100-00. SAND2011-3779. Albuquerque, NM: Sandia National Laboratories; 2011.

[31] Cousins DS, Suzuki Y, Murray RE, Samaniuk JR, Stebner AP. Recycling glass fiber thermoplastic composites from wind turbine blades. Journal of Cleaner Production. 2019;209:1252–63.

[32] Cooperman A, Eberle A, Lantz E. Wind turbine blade material trends and projections. Wind Energy. 2021;24(10):1067–84.

[33] Adnan M, Ahmad J, Ali SF. A comprehensive review on renewable energy projects in Pakistan.

Environmental Science and Pollution Research. 2022;29:63640–61.

[34] Khalid M, Akram U, Shafiq S. Wind power potential and economic analysis of wind energy development in Pakistan. Renewable and Sustainable Energy Reviews. 2023;175:113184.

[35] Government of Pakistan. Alternative and Renewable Energy Policy 2019. Islamabad: Ministry of Energy (Power Division); 2019.

[36] Ahmed S, Mahmood M, Hasan A, Siddique GA. Economic viability of wind power in Pakistan. Energy Policy. 2020;142:111458.

[37] Hassan SA, Kalair AR, Abas N, Saleem MS. Pakistan wind energy scenario, issues and way forward. Energy, Ecology and Environment. 2019;4(3):117–28.

[38] Bhutto AW, Bazmi AA, Zahedi G. Greener energy: issues and challenges for Pakistan—wind power prospective. Renewable and Sustainable Energy Reviews. 2013;20:519–38.

[39] Drela M. XFOIL: An analysis and design system for low Reynolds number airfoils. In: Mueller TJ, editor. Low Reynolds Number Aerodynamics. Lecture Notes in Engineering, vol 54. Berlin: Springer; 1989. p. 1–12.

[40] Marten D, Wendler J, Pechlivanoglou G, Nayeri CN, Paschereit CO. QBlade: an open source tool for design and simulation of horizontal and vertical axis wind turbines. International Journal of Emerging Technology and Advanced Engineering. 2013;3(3):264–9.

[41] Hand MM, Simms DA, Fingersh LJ, Jager DW, Cotrell JR, Schreck S, et al. Unsteady Aerodynamics Experiment Phase VI: Wind Tunnel Test Configurations and Available Data Campaigns. NREL/TP-500-29955. Golden, CO: NREL; 2001.